Supporting Information

Simulation-Guided Design of Solar Steam Generator Arrays for Efficient All-Cold Evaporation under Natural Sunlight

Ke Shao,[a] Jingjing Li,[a] Jun Zhao,[a] Suxu Wang,[a] Yi Lu,[b] Petri Murto,[c,d] Zhihang Wang,*[,e,f] & Xiaofeng Xu*[,a]

[a] College of Materials Science and Engineering, Ocean University of China, Qingdao 266100, China.

[b] Jiangsu Co-Innovation Center of Efficient Processing and Utilization of Forest Resources, International Innovation Center for Forest Chemicals and Materials, College of Science, Nanjing Forestry University, Nanjing 210037, China

[c] Department of Chemistry and Materials Science, Aalto University, Kemistintie 1, 02150 Espoo, Finland.

[d] Yusuf Hamied Department of Chemistry, University of Cambridge, Cambridge, CB2 1EW, United Kingdom.

[e] School of Engineering, College of Science and Engineering, University of Derby, Markeaton Street, Derby DE22 3AW, United Kingdom.

[f] Department of Materials Science and Metallurgy, University of Cambridge, Cambridge, CB3 0FS, United Kingdom.

* Corresponding authors: X. Xu, email: xuxiaofeng@ouc.edu.cn

Z. Wang, email: zw428@cam.ac.uk

Table of Contents

1. Materials S4
2. Characterizations S4
3. Numerical simulation S5
4. Stability of balsa wood S6
5. Structural integrity characterization S6
6. Absorption characterization S7
7. Fiber diameter distribution S7
8. Macro photography S8
9. Contact angle measurements S8
10. Temperature distribution simulation S9
11. Evaporation contribution characterization S9
12. Energy balance analysis S10
13. Solar desalination characterization S13
14. Boundary condition of air velocity and RH distribution simulation S14
15. Physical modeling and mesh generation of SGs S15
16. Airflow distribution simulation across SGs S16
17. RH distribution simulation across SGs S17
18. Mesh generation of SG arrays S18
19. Process schematic of particle distribution simulation S18
20. Air particle distribution simulation S19
21. Environment parameters under a real sky S22
22. Water evaporation characterization under real sky S23
23. Outdoor evaporation of neat water S26
24. Outdoor clean water production S26
25. Water quality characterization S27
26. Reference S27

1. Materials

Commercially available balsa wood was used to fabricate the side fins for three-dimensional (3D) interfacial steam generators (SGs). Polyurethane-based 2D fabrics were prepared through electrospinning, which was used as the photothermal layer. The 3D scaffold was printed based on active foaming polylactic acid (PLA).

2. Characterizations

Contact angles were measured via a contact angle goniometer (JC2000DM, Powereach) by using 4 μL of water droplet as an indicator. The absorption spectra were obtained from a UV−Vis−NIR spectrometer (LAMBDA 1050+, PerkinElmer) with an integrating sphere. The absorptance at each wavelength is defined by $1 - T - R$, where T and R are the corresponding transmittance and reflectance, respectively. The densities, porosity and saturated water contents were measured by using a high-precision density meter (AU-120PF, Quarrz). The morphologies and elemental mapping were characterized by a scanning electron microscope (VEGA3, TESCAN) in combination with energy dispersive X-ray spectrometry. The air velocity was monitored by using a hotline anemometer (AR866A, Sima). The outdoor evaporation experiments were conducted in July at Ocean University of China, Qingdao, China.

3. Numerical simulation

The velocity magnitude, relative humidity distribution, heat transfer and particle distribution were simulated using COMSOL Multiphysics software 6.1 version. A multi-physics module of Turbulent Flow, Moisture Transport, Heat transfer and Particle Tracing for Fluid Flow module was used to evaluate the evaporative dynamics of SG with different numbers of fins as enabled by the different convective flow speeds. The velocity magnitude was simulated by solving the following equations,[1]

$$\mathrm{Re_w} = \frac{\rho|\mathrm{u}|\varsigma_\mathrm{w}}{\mu} = \frac{|\mathrm{u}|}{\mu_\tau}\cdot\frac{\rho\mu_\tau\varsigma_\mathrm{w}}{\mu} = \mathrm{u}^+\varsigma_\mathrm{w}{}^+, \mathrm{u}^+ = f\left(\varsigma_\mathrm{w}{}^+\right) \quad \text{(S1)}$$

$$\nabla G\cdot\nabla G + \sigma_w G\left(\nabla\cdot\nabla G\right) = \left(1+2\sigma_w\right)G^4, \sigma_w = \frac{1}{G} - \frac{\varsigma_{ref}}{2} \quad \text{(S2)}$$

$$\mu_T = \mu\left(\left(\frac{df}{d\varsigma_\mathrm{w}{}^+}\right)^{-1} - 1\right) \quad \text{(S3)}$$

where $\mathrm{Re_w}$ is wall Reynolds number, u is the velocity field, ρ is the density of the fluid, μ is the dynamic viscosity, u^+ is dimensionless velocity, $\varsigma_\mathrm{w}{}^+$ is dimensionless wall shear stress, σ_w is an argument in the wall function, ς_{ref} is reference stress, G is the reciprocal wall distance, μ_T is turbulent viscosity.

4. Stability of balsa wood

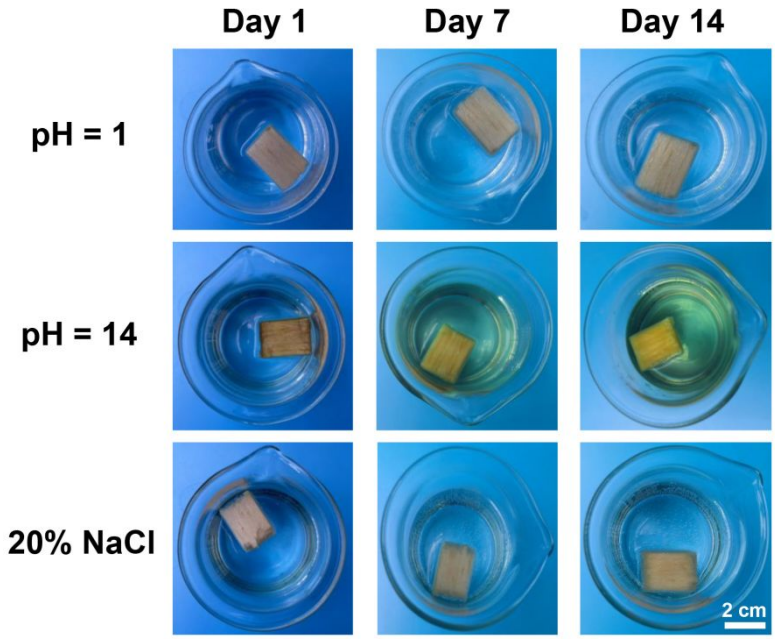

Figure S1. Balsa wood sheets immersed in extreme water conditions.

5. Structural integrity characterization

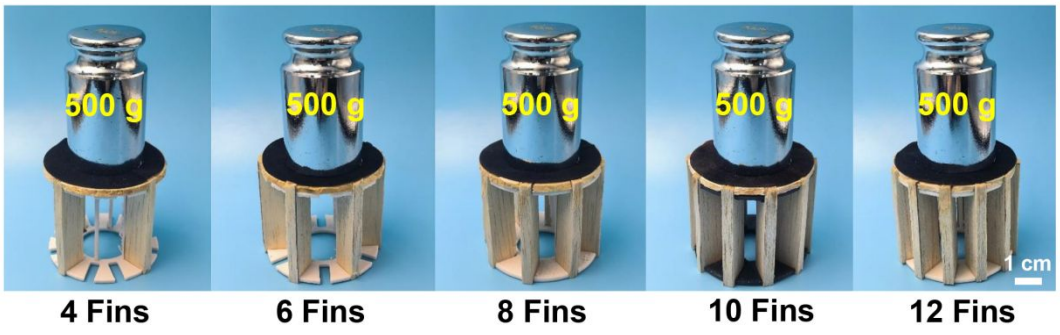

Figure S2. Images of all SGs sustaining a weight of 500 g.

6. Absorption characterization

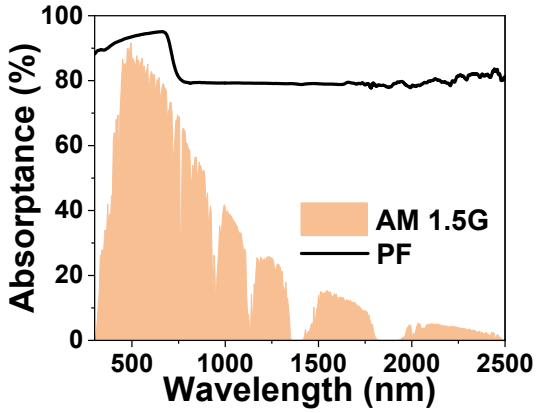

Figure S3. Absorption spectrum of the photothermal fabric.

The transmission and reflection spectra of the aerogel matrix over the whole solar spectrum (250 − 2500 nm) were measured using an UV−Vis−NIR spectrophotometer equipped with an integrating sphere. According to Kirchhoff's law, the absorption spectrum can be obtained through the formula: A = 1 − R − T. Therefore, the absorptance (At) of the aerogel matrix across the full solar spectrum can be calculated using equation S1,[2]

$$A_t = \frac{\int A \cdot S \cdot d\lambda}{\int S \cdot d\lambda} \times 100\% \qquad \text{(S4)}$$

where S is solar spectral irradiance (W m^{-2} nm^{-1}) and λ is wavelength (nm).

7. Fiber diameter distribution

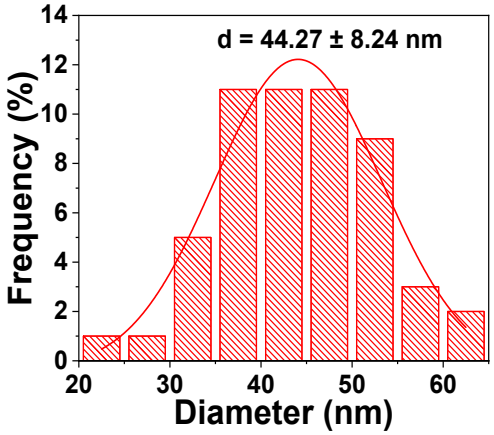

Figure S4. Fiber diameter distribution of the photothermal fabric.

8. Macro photography

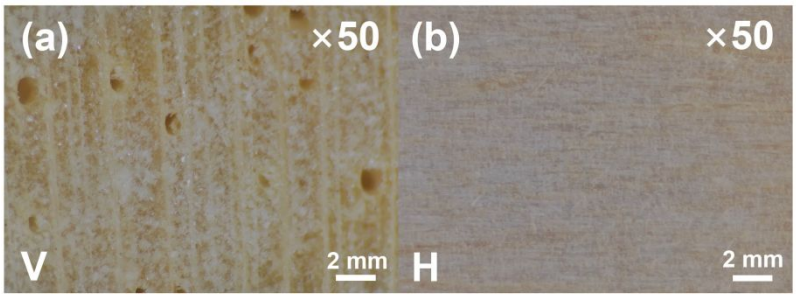

Figure S5. Microscopic photographs of balsa wood along (a) vertical (V) and (b) horizontal (H) growth directions.

9. Contact angle measurements

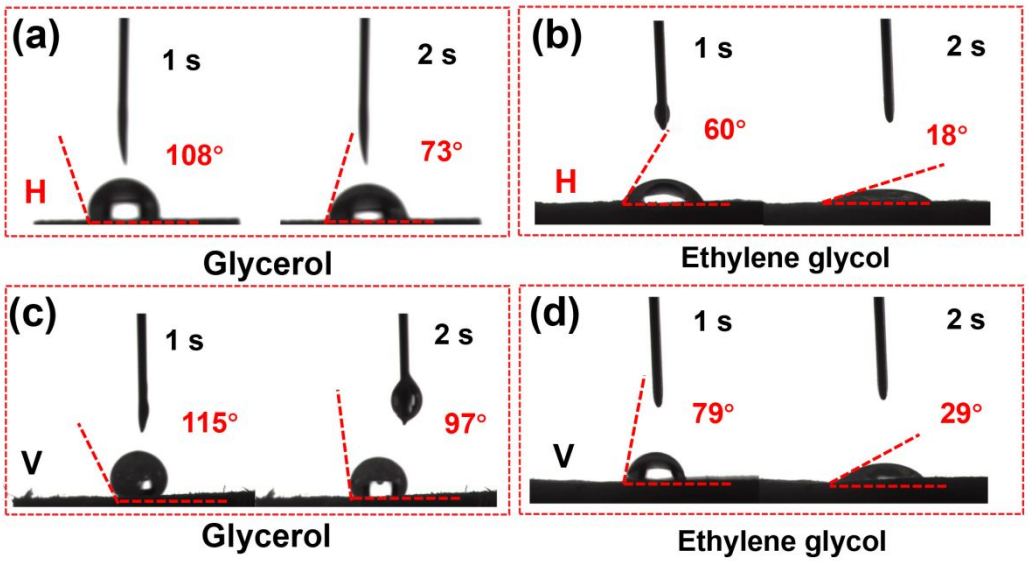

Figure S6. Contact angle (CA) measurements of (a) (b) transverse and (c) (d) longitudinal cross-sections of balsa wood in different organic solvents.

10. Temperature distribution simulation

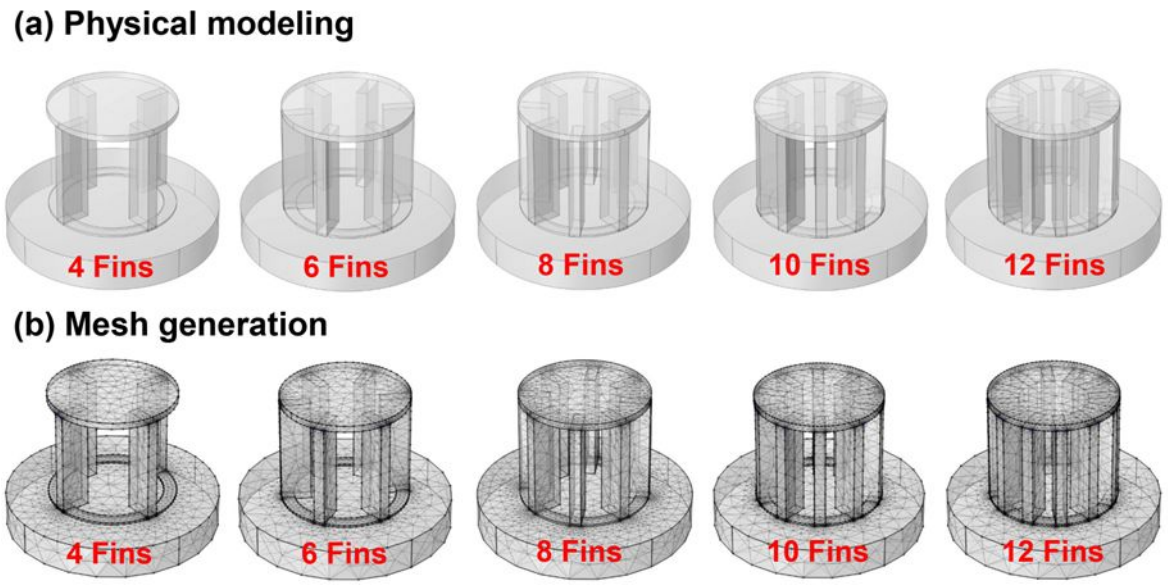

Figure S7. Temperature distribution simulation: (a) physical modeling and (b) mesh generation of five SGs.

11. Evaporation contribution characterization

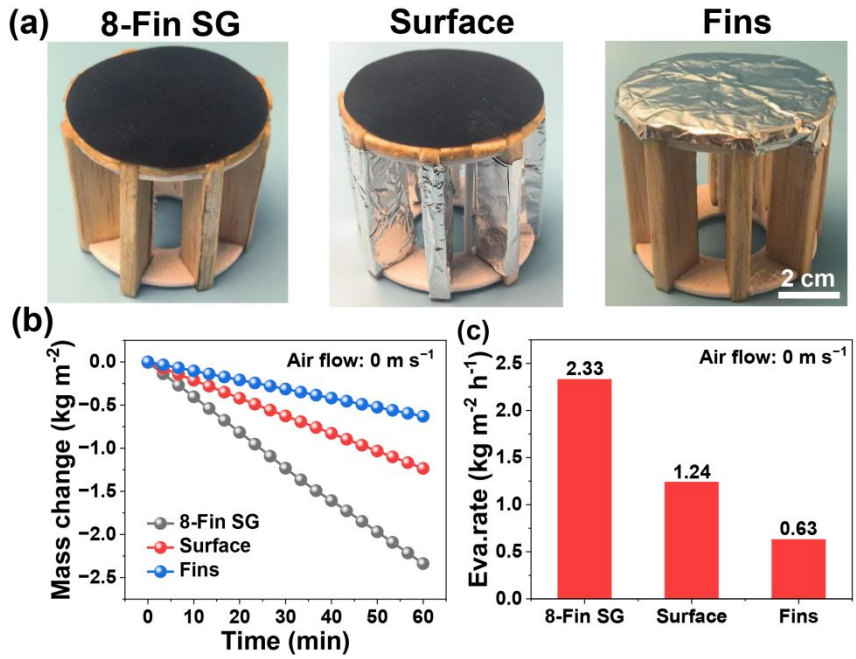

Figure S8. (a) Digital photographs, (b) mass changes of water and (c) evaporation rates of different devices.

12. Energy balance analysis

a) Radiation

The radiation loss was analyzed by Stefan-Boltzmann equation S5,[3]

$$\Phi = \varepsilon A\sigma\left(T_1^4 - T_2^4\right) \qquad \text{(S5)}$$

Φ is heat flux (W), ε denotes emissivity (Supposing the evaporator has a maximum emissivity of 1), A is evaporation surface area, σ represents the Stefan-Boltzmann constant (σ = 5.670373×10^{-8} W m^{-2} K^{-4}).[4]

b) Conduction

The heat conduction was analyzed according to the following equation S6,[5]

$$Q = Cm\Delta T \qquad \text{(S6)}$$

Q denotes the heat energy, C is the specific heat capacity of pure water (4.2 J g^{-1} K^{-1}), m represents the weight of bulk water and ΔT is the reduced temperature of the bulk water after stable steam generation.

c) Convection

The convection was calculated by Newton's law of cooling S7,[6]

$$Q = hA\Delta T \qquad \text{(S7)}$$

Q is the heat energy, h denotes the convection heat transfer coefficient (~5 W m^{-2} K^{-1}).[7] A represents surface area. ΔT is difference between the ambient temperature around the evaporator and the surface temperature of the evaporator.

d) Reflection

The solar absorption of solar absorber is 91.4%; thus, the refection loss is ~8.6%.

e) Evaporation

The evaporation heat of water is calculated using the following equation S8 and S9,[8]

$$P = \mathrm{m}\left(\mathrm{h}_{LV} + Q\right) \quad \text{(S8)}$$

$$Q = C\Delta T \quad \text{(S9)}$$

where m is the evaporation rate, h_{LV} is the latent heat of total enthalpy used for the transition of water from liquid to vapor phase, Q is the sensible heat of water, C is the specific heat capacity of pure water (4.2 J g^{-1} K^{-1}), ΔT is the temperature difference between the initial temperature and the evaporation temperature.

Recycled energy = Total output − Total input

Total output = Vapor output + Convection output (top surface to air) + Radiation output (top surface to air)

Total input = Solar input + Environment input

Environment input = Convection input (air to fins) + Radiation input (air to fins) + Conduction input (water to fins)

Table S1. An analysis of energy losses and gains of 8-Fin SG during solar evaporation.

Ambient Temperature (K)	301.15
Top surface area (m^2)	2.83×10^{-3}
Fins area (m^2)	1.23×10^{-2}
Stable top temperature (K)	310.45
Stable temperature of fins (K)	299.35
Initial water temperature (K)	300.85
Stable water temperature (K)	299.85
Optical absorption coefficient (%)	91.4
Vapor output (W)	4.48
Convection output (W)	0.13
Radiation output (W)	0.17
Solar input (W)	2.58
Radiation input (W)	0.14
Convection input (W)	0.10
Conduction input (W)	0.20
Total input (W)	3.02
Total output (W)	4.78
Recycle energy (W)	1.76

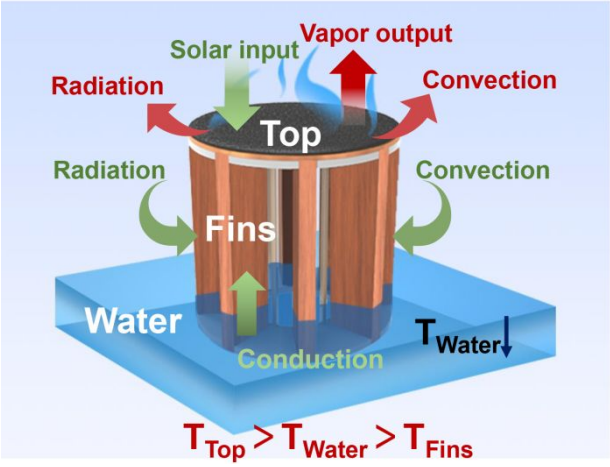

Figure S9. Schematic diagram of heat transfer pathways of 8-Fin SG during indoor solar evaporation.

13. Solar desalination characterization

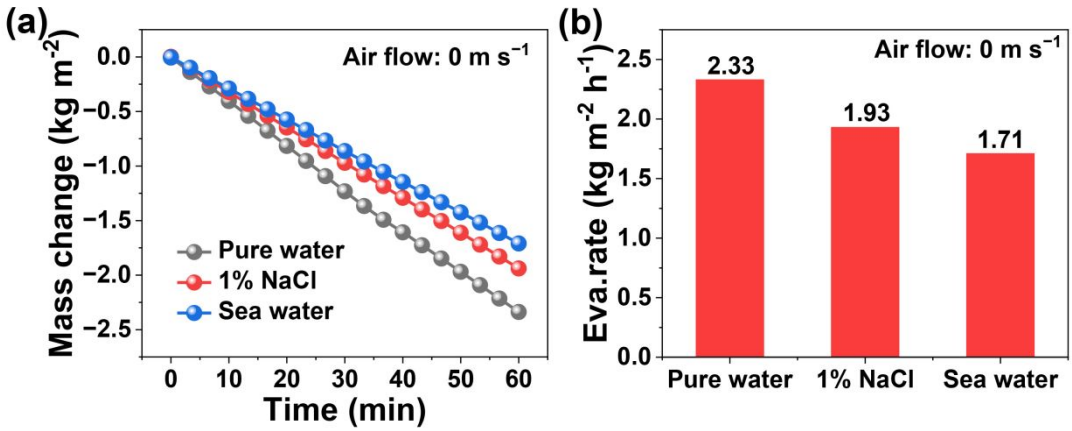

Figure S10. (a) Mass changes and (b) evaporation rate of water of 8-Fin SG in fresh water, 1% NaCl solution and sea water over 1 h under windless and 1 sun conditions.

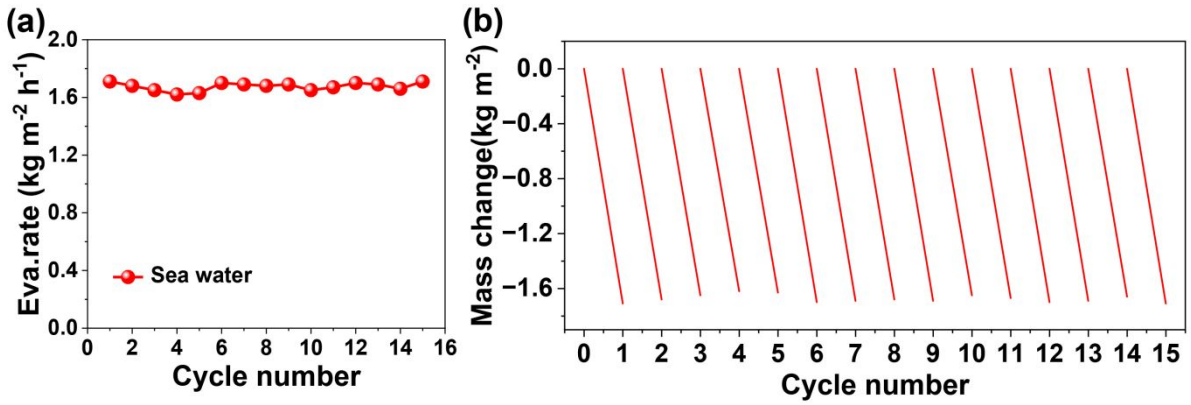

Figure S11. (a) Evaporation rate and (b) mass changes of cyclic solar desalination under windless and 1 sun conditions.

14. Boundary condition of air velocity and RH distribution simulation

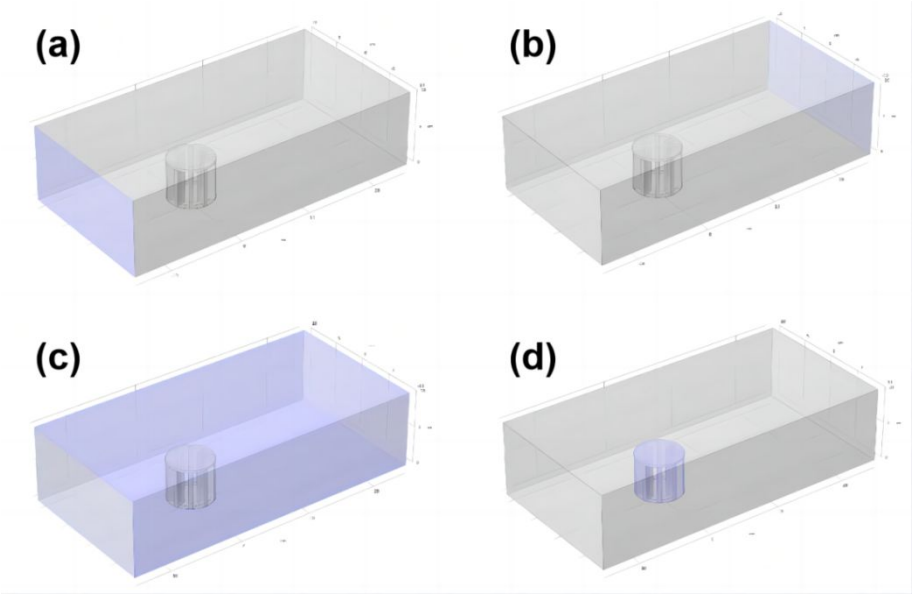

Figure S12. Boundary conditions in air velocity and RH distribution simulation of SG: convective flow (a) inlet and (b) outlet, (c) vapor outlet and (d) evaporation flux of SG.

15. Physical modeling and mesh generation of SGs

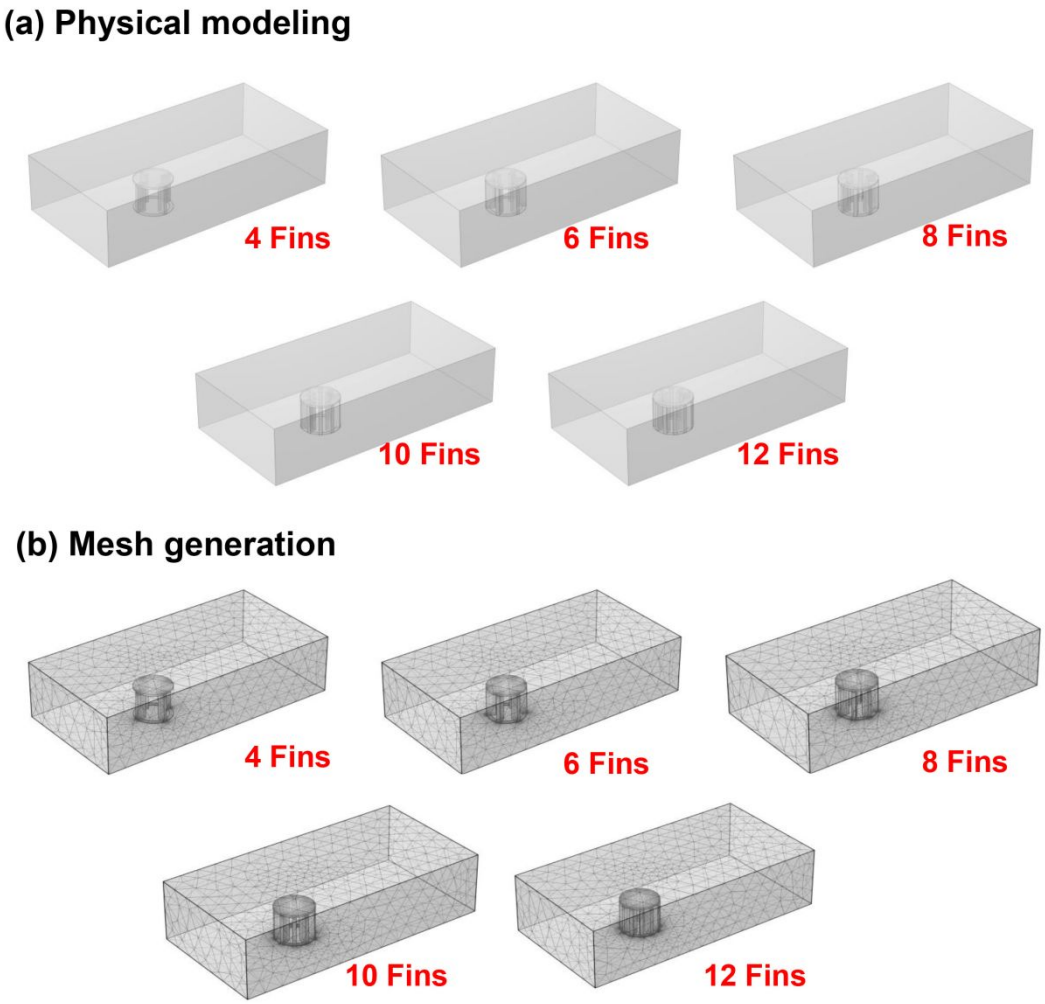

Figure S13. Air velocity and RH distribution simulation: (a) physical modeling and (b) mesh generation of five SGs.

16. Airflow distribution simulation across SGs

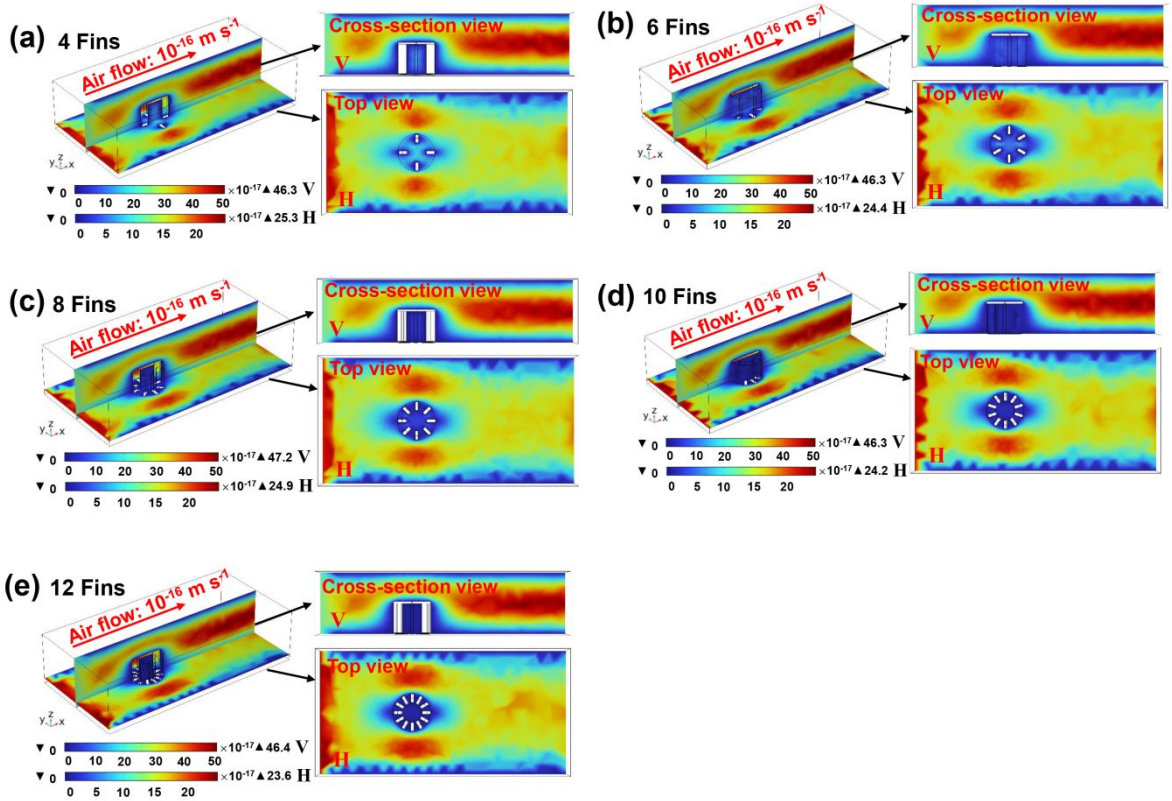

Figure S14. Airflow distributions across five SGs with varying fin number under calm (air velocity: 10^{-16} m s^{-1}) and 1 sun conditions: (a) 4 Fins, (b) 6 Fins, (c) 8 Fins, (d) 10 Fins and (e) 12 Fins.

17. RH distribution simulation across SGs

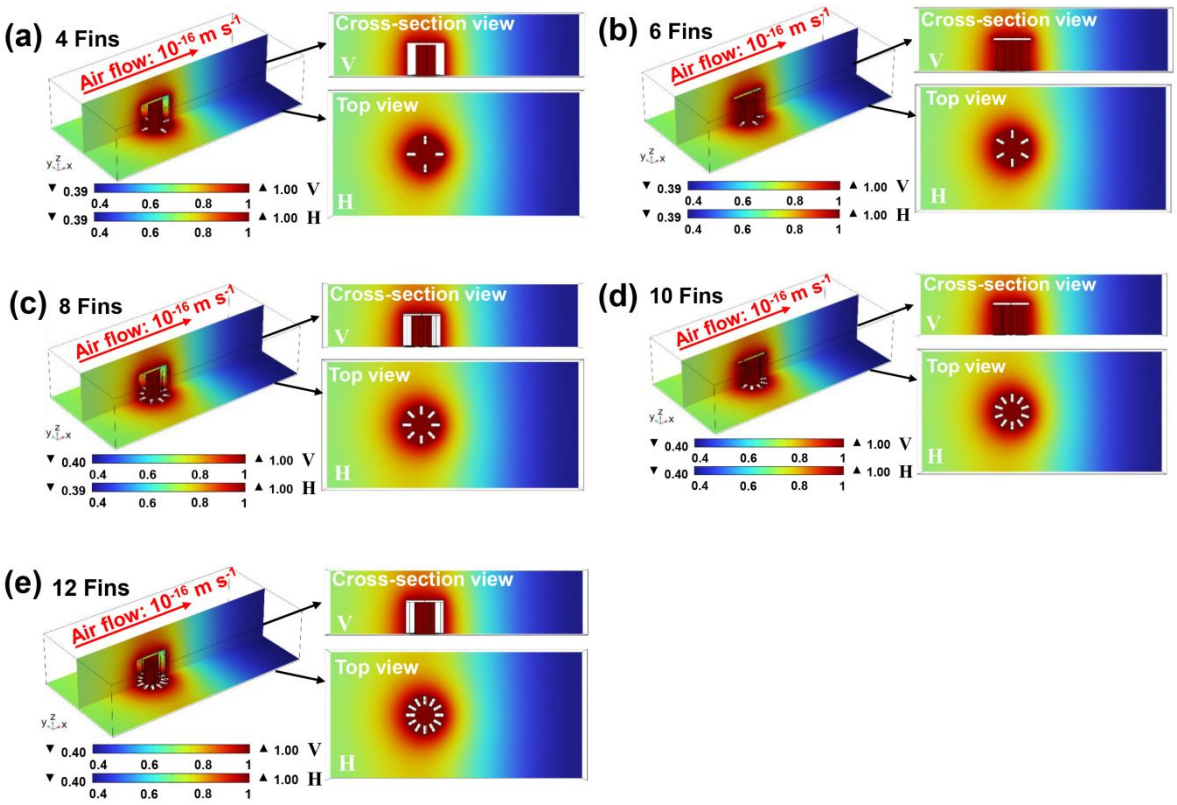

Figure S15. RH distributions across five SGs with varying fin number under calm (air velocity: 10^{-16} m s^{-1}) and 1 sun conditions: (a) 4 Fins, (b) 6 Fins, (c) 8 Fins, (d) 10 Fins and (e) 12 Fins.

18. Mesh generation of SG arrays

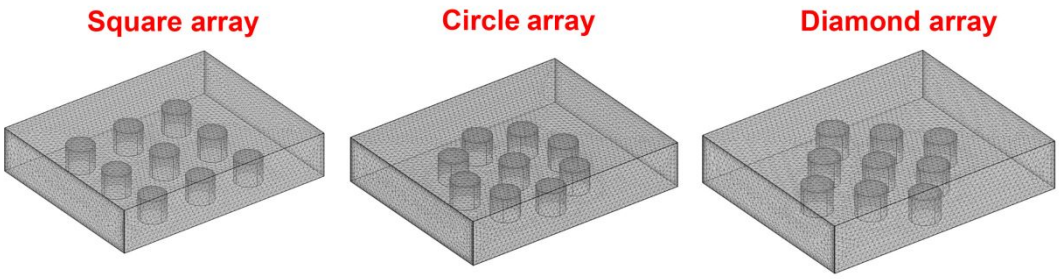

Figure S16. Particle distribution simulation mesh generation across square, circular and diamond arrays.

19. Process schematic of particle distribution simulation

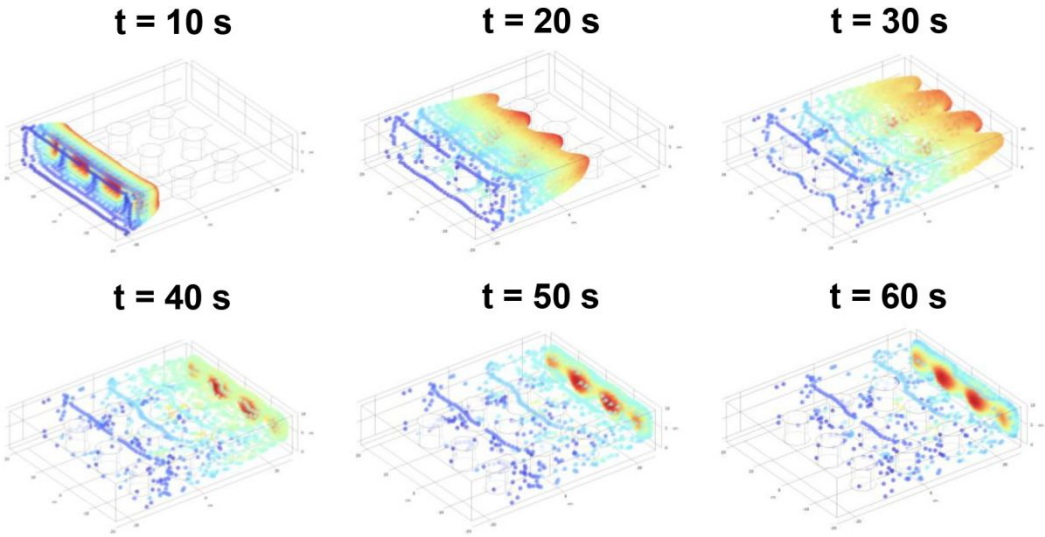

Figure S17. Particle distribution at t = 10, 20, 30, 40, 50, 60 for a convective velocity (air velocity: 0.01 m s^{-1}).

20. Air particle distribution simulation

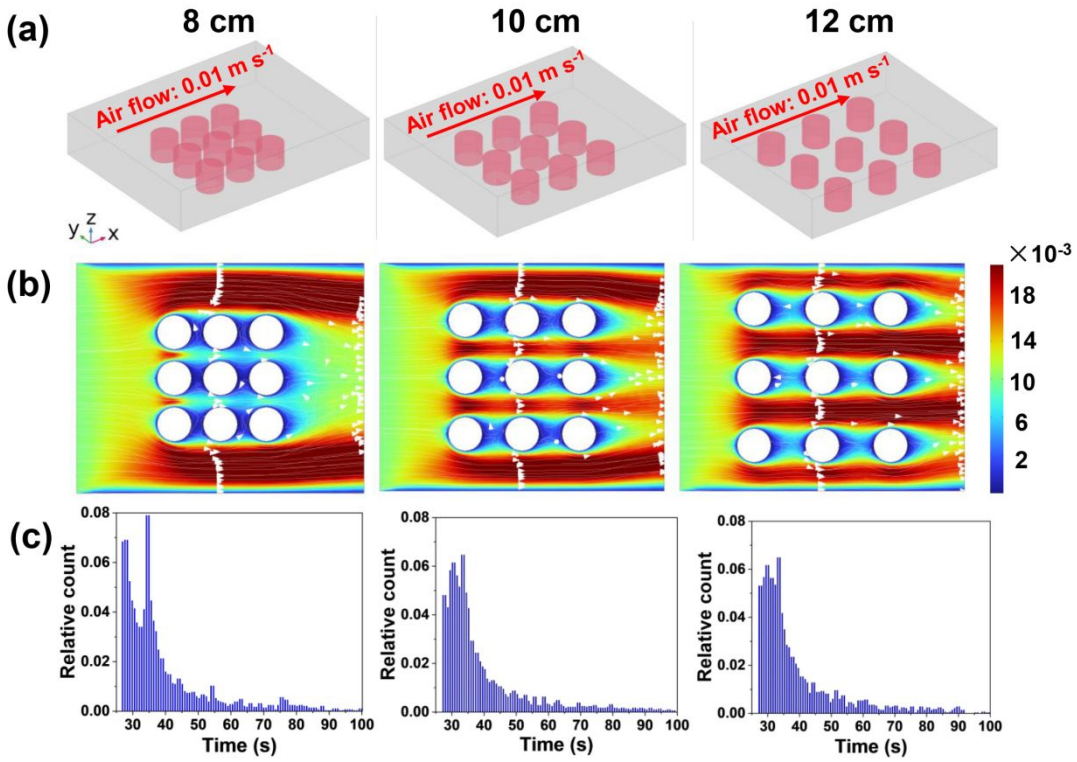

Figure S18. (a) Geometric modeling of square arrays (spacing distance: 8, 10 and 12 cm) based on 8-Fin SGs. Simulations of (b) air flow distribution and (c) dwell time distribution of air particles across square arrays under a light breeze (air velocity: 0.01 m s^{-1}).

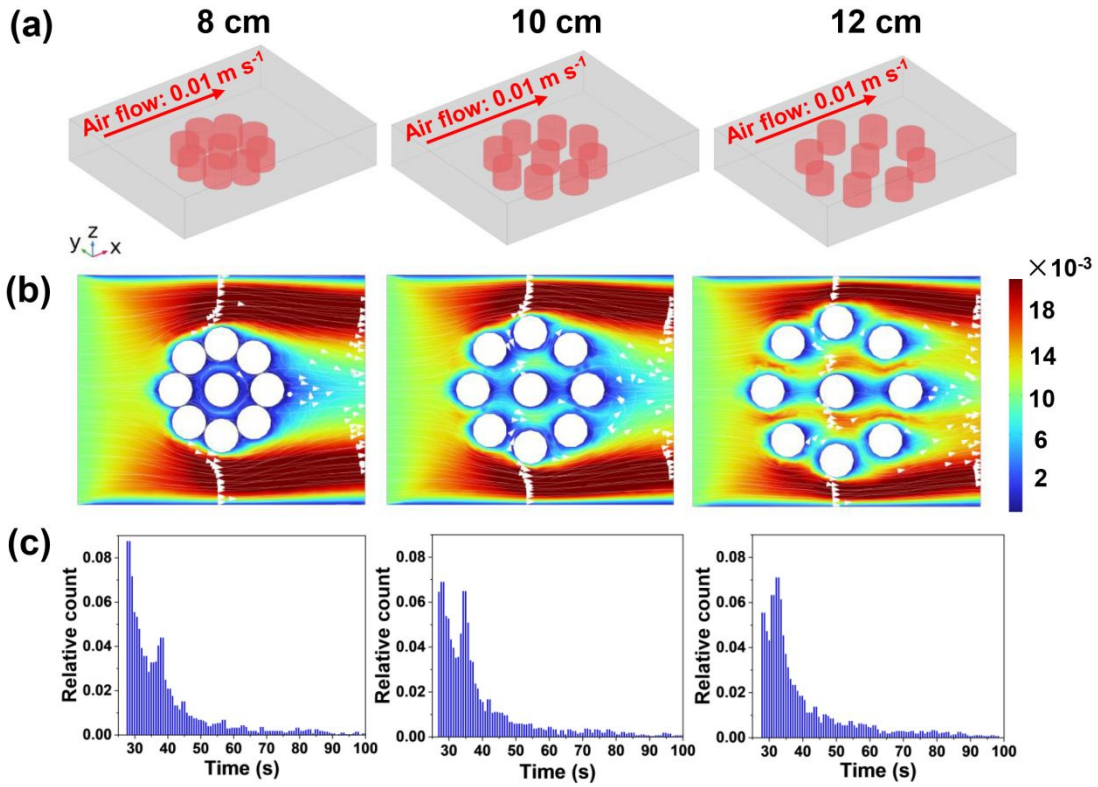

Figure S19. (a) Geometric modeling of circular arrays (spacing distance: 8, 10 and 12 cm) based on 8-Fin SGs. Simulations of (b) air flow distribution and (c) dwell time distribution of air particles across circular arrays under a light breeze (air velocity: 0.01 m s^{-1}).

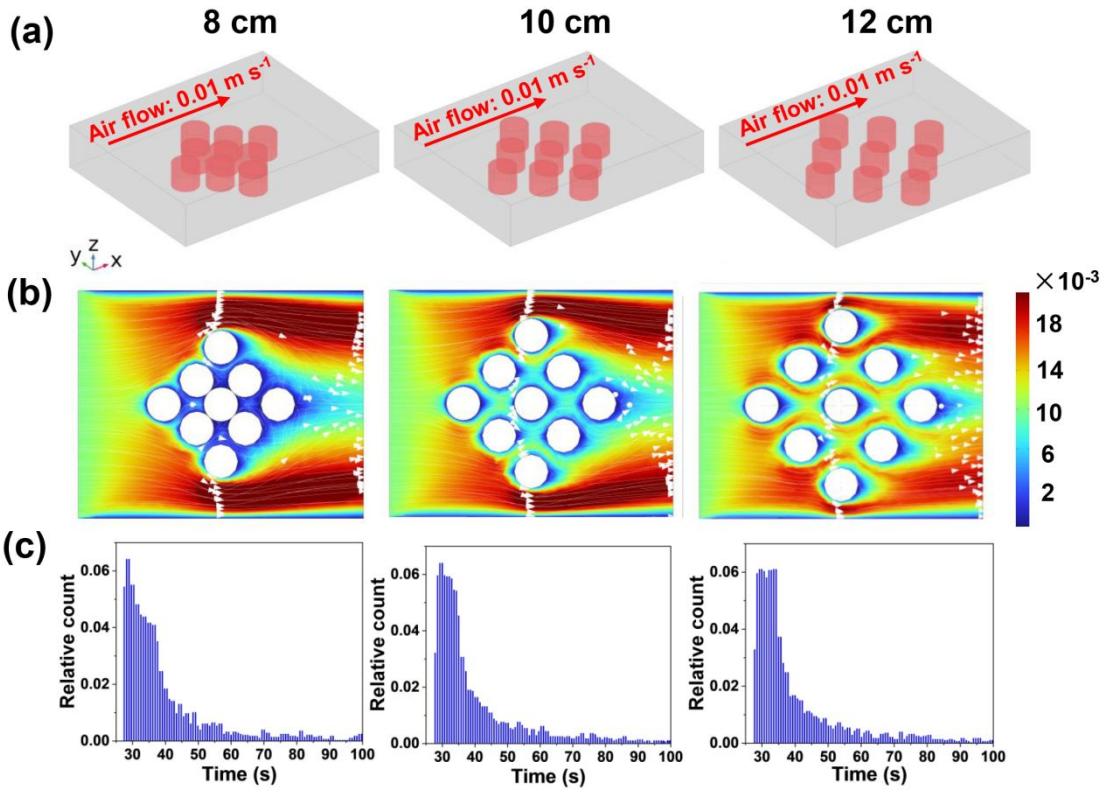

Figure S20. (a) Geometric modeling of diamond arrays (spacing distance: 8, 10 and 12 cm) based on 8-Fin SGs. Simulations of (b) air flow distribution and (c) dwell time distribution of air particles across diamond arrays under a light breeze (air velocity: 0.01 m s^{-1}).

21. Environment parameters under a real sky

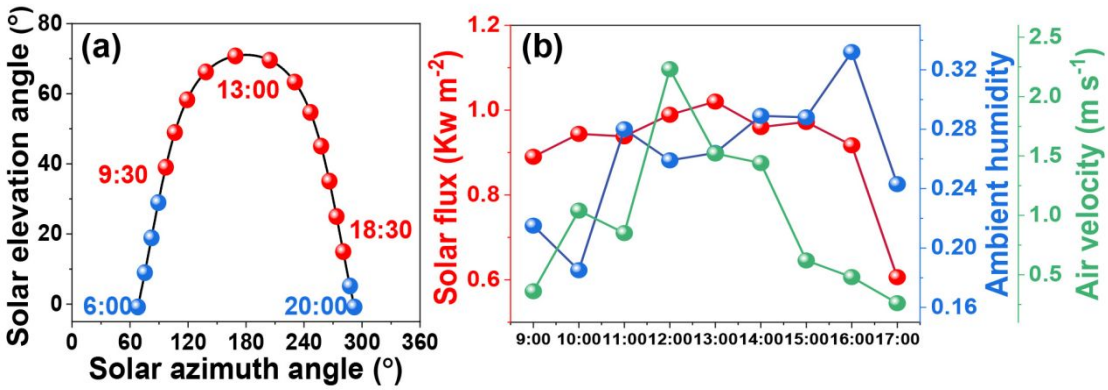

Figure S21. (a) The Sun's position on the sky dome. (b) Synchronous solar intensity, ambient humidity and air velocity at outdoor measurements.

22. Water evaporation characterization under real sky

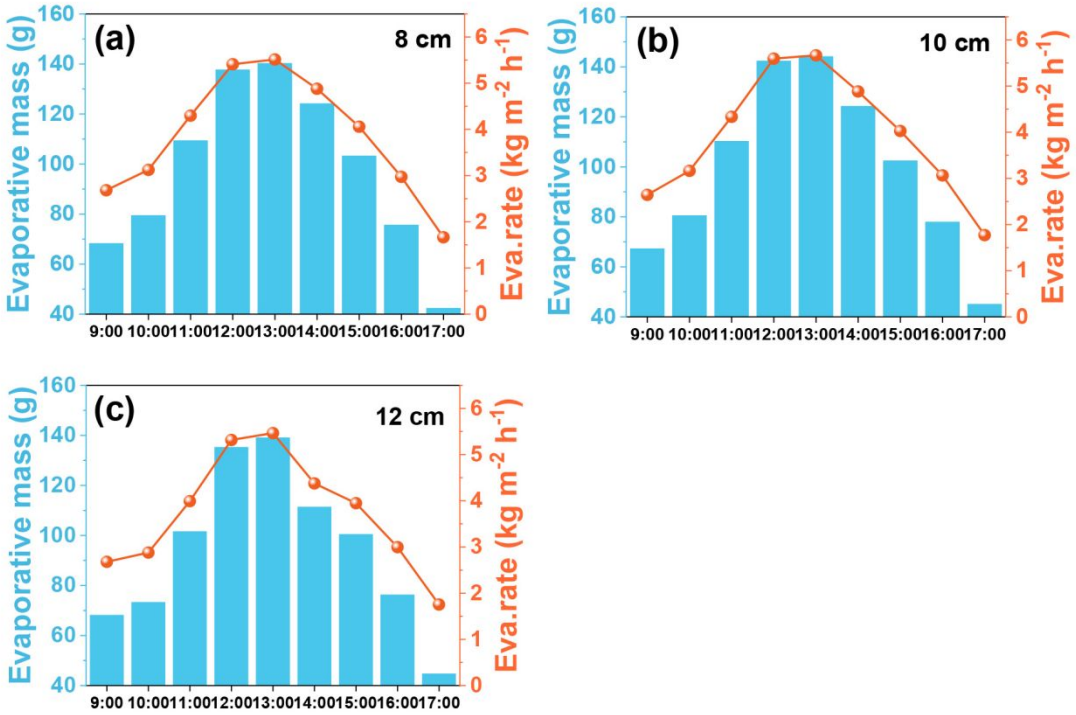

Figure S22. Water evaporation of square arrays with different spacing distance: (a) 8 cm, (b) 10 cm and (c) 12 cm.

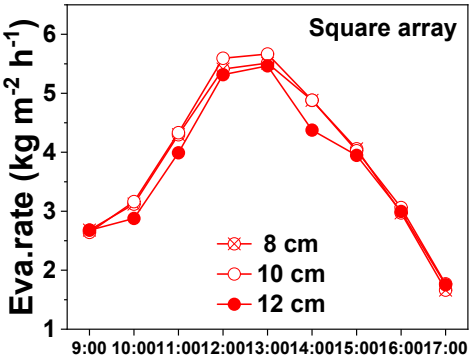

Figure S23. Summary of water evaporation rates of square arrays (spacing distance: 8, 10, 12 cm) in the daytime.

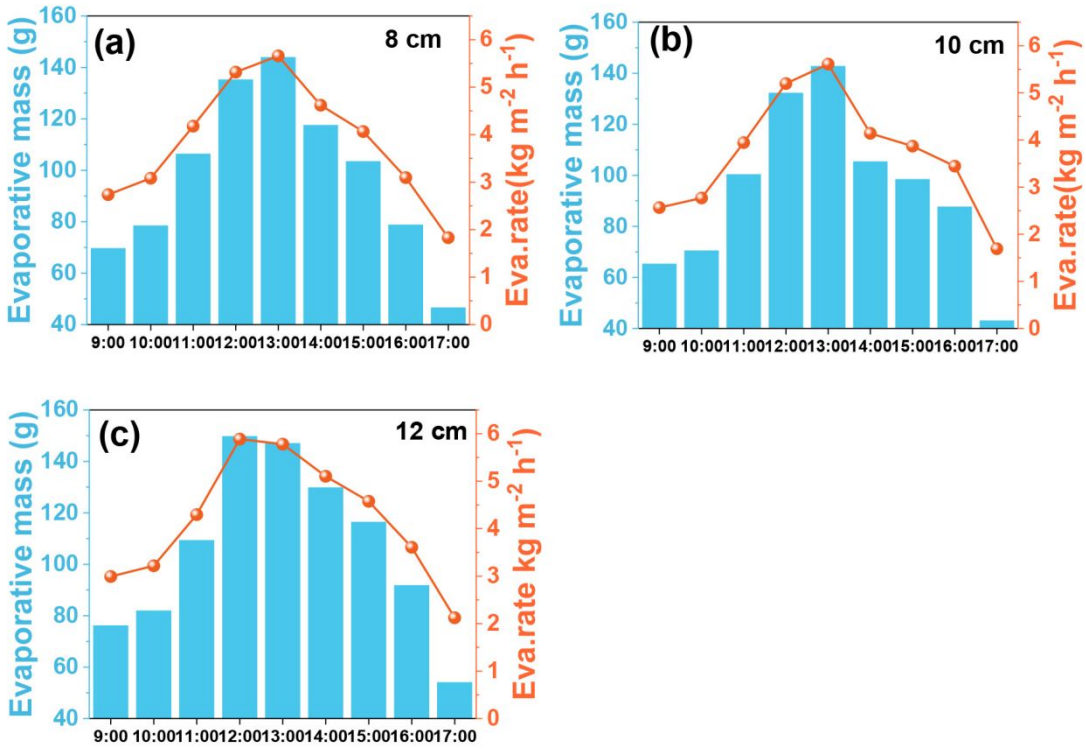

Figure S24. Water evaporation of circular arrays with different spacing distance: (a) 8 cm, (b) 10 cm and (c) 12 cm.

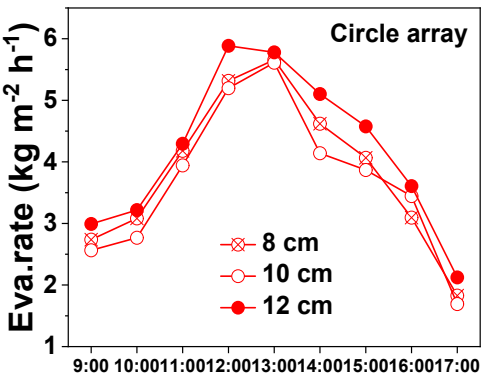

Figure S25. Summary of water evaporation rates of circular arrays (spacing distance: 8, 10 and 12 cm) in the daytime.

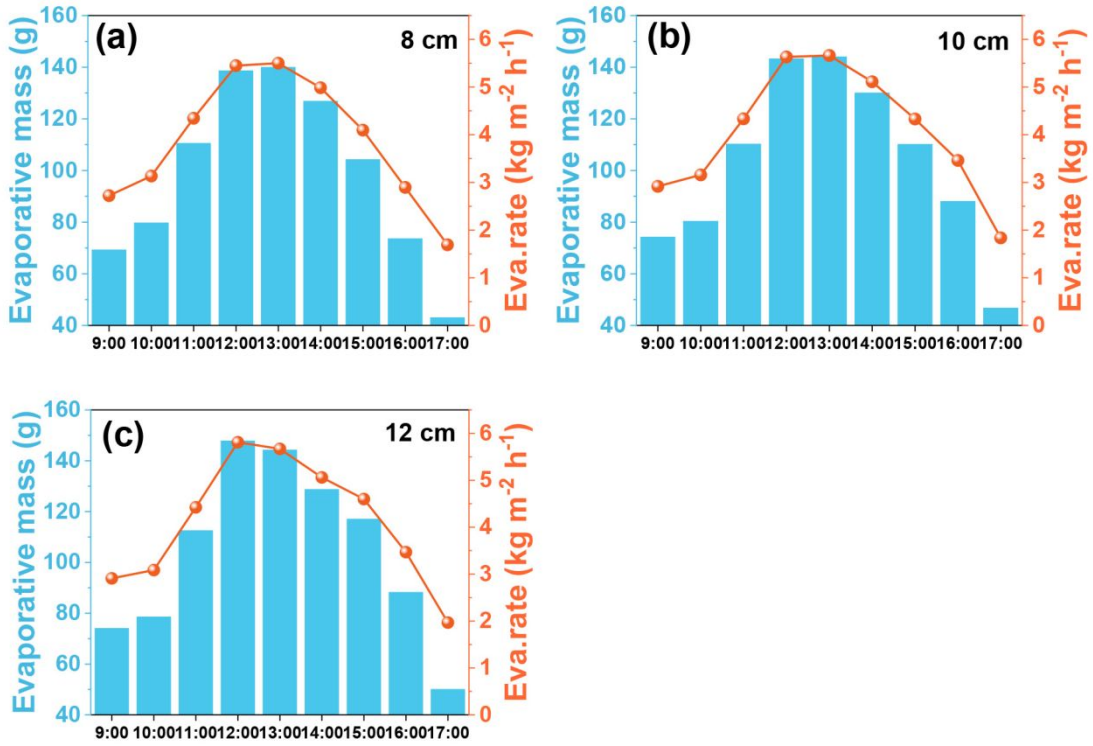

Figure S26. Water evaporation of diamond arrays with different spacing distance: (a) 8 cm, (b) 10 cm and (c) 12 cm.

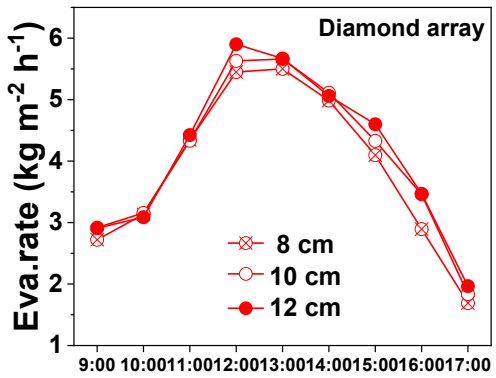

Figure S27. Summary of water evaporation rates of circular arrays (spacing distance: 8, 10 and 12 cm) in the daytime.

23. Outdoor evaporation of neat water

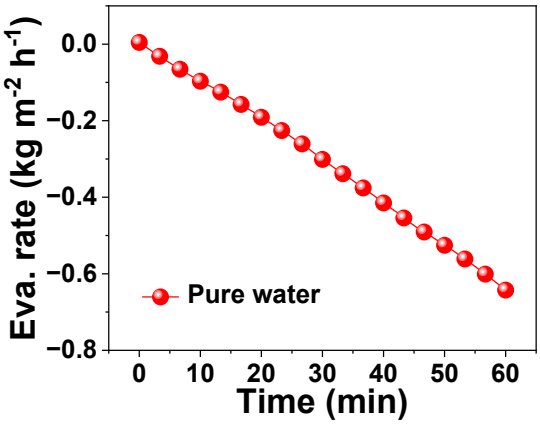

Figure S28. Evaporation of neat water under real sky at noon (12:00 − 13:00).

24. Outdoor clean water production

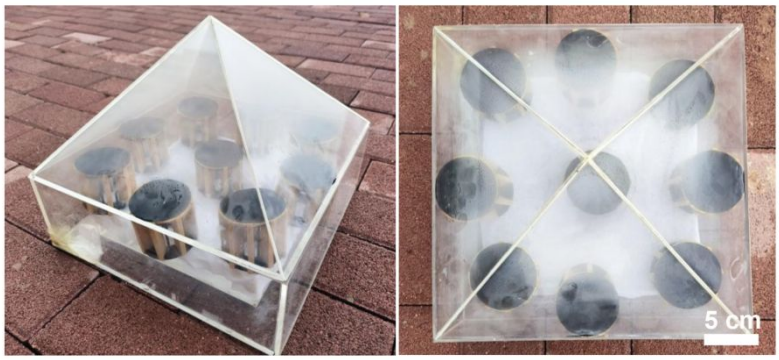

Figure S29. Digital photographs of clean water production device.

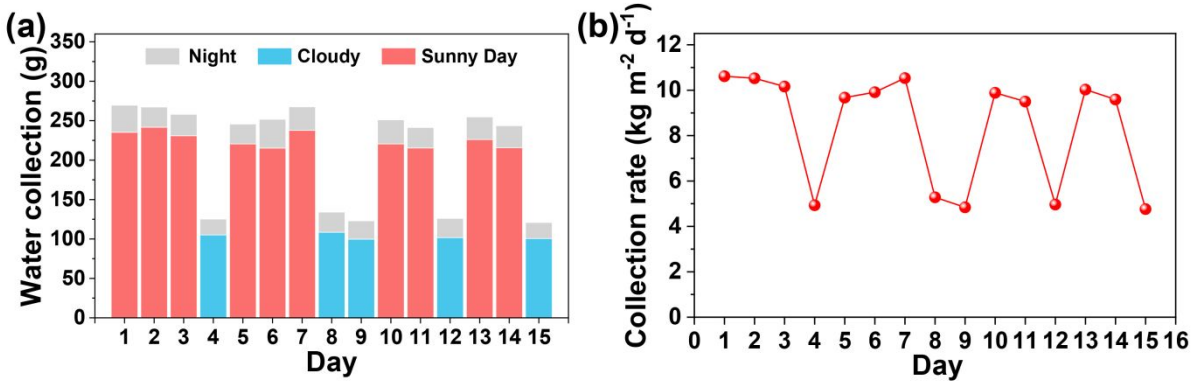

Figure S30. (a) Clean water yields and (b) rates of the device under real sky over 15 days.

25. Water quality characterization

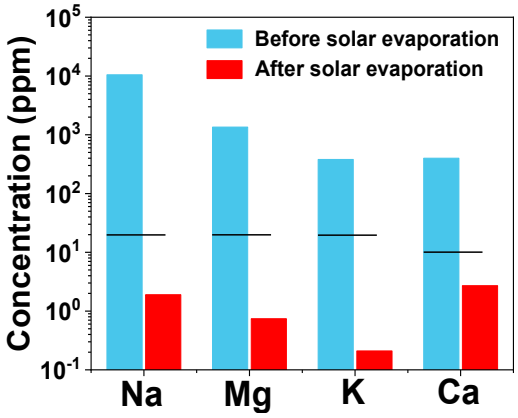

Figure S31. Concentrations of primary elements in water before and after solar evaporation. (The black lines indicate WHO quality standards for safe drinking water.)

26. Reference

[1] Y. Wang, X. Wu, T. Gao, Y. Lu, X. Yang, G.Y. Chen, G. Owens, H. Xu, Same materials, bigger output: A reversibly transformable 2D–3D photothermal evaporator for highly efficient solar steam generation, Nano Energy 79 (2021) 105477.

[2] S. Gong, T. He, D. Zhu, A. Sundaramurthy, Q. Li, X. Shu, Preparation of ATO-incorporated composite latex with tailored structure and controllable size for highly spectrum-selective applications, Mater. Des 180 (2019) 107919.

[3] N. Li, L. Qiao, J. He, S. Wang, L. Yu, P. Murto, X. Li, X. Xu, Solar-Driven Interfacial Evaporation and Self-Powered Water Wave Detection Based on an All-Cellulose Monolithic Design, Adv. Funct. Mater. 31 (2020) 2008681.

[4] J. Gao, K. Shao, J. Li, N. Li, S. Wang, X. Wu, P. Murto, Z. Wang, Y. Zhou, X. Xu, Foaming photothermal inks for direct-ink writing: hierarchical design and enhanced solar-powered interfacial evaporation, J. Mater. Chem. A 12 (2024) 6592-6609.

[5] J. Zhou, Y. Gu, P. Liu, P. Wang, L. Miao, J. Liu, A. Wei, X. Mu, J. Li, J. Zhu, Development and Evolution of the System Structure for Highly Efficient Solar Steam Generation from Zero to Three Dimensions, Adv. Funct. Mater. 29 (2019) 1903255.

[6] X. Li, B. Zhu, J. Zhu, Graphene oxide based materials for desalination, Carbon 146 (2019) 320-328.

[7] H. Ghasemi, G. Ni, A.M. Marconnet, J. Loomis, S. Yerci, N. Miljkovic, G. Chen, Solar steam generation by heat localization, Nat. Commun. 5 (2014) 4449.

[8] D. Wei, C. Wang, G. Shi, J. Zhang, F. Wang, P. Tan, Z. Zhao, Y. Xie, Enabling Self-Adaptive Water-Energy-Balance of Photothermal Water Diode Evaporator: Dynamically Maximizing Energy Utilization Under the Ever-Changing Sunlight, Adv. Mater. 36 (2024) e2309507.